Hexagons and squares in a passive nonlinear optical system

J. B. Geddes, R. A. Indik, and J. V. Moloney
Department of Mathematics, University of Arizona, Tucson, Arizona 85721

W. J. Firth
Department of Physics and Applied Physics, University of Strathclyde, Glasgow G4 0NG, Scotland
(Received 19 November 1993)

Pattern formation is analyzed and simulated in a nonlinear optical system involving all three space dimensions as well as time in an essential way. This system, counterpropagation in a Kerr medium, is shown to lose stability, for sufficient pump intensity, to a nonuniform spatial pattern. We observe hexagonal patterns in a self-focusing medium, and squares in a self-defocusing one, in good agreement with analysis based on symmetry and asymptotic expansions.

PACS number(s): 42.65.−k, 42.50.Ne

I. INTRODUCTION

Spontaneous pattern formation is a topic of great current interest across many fields of science [1,2]. Nonlinear optics is particularly interesting in this field [3,4] because optical patterns invite both applications and fundamental interest, the latter extending into the quantum domain [5].

Communications and information-processing applications have stimulated much progress in the field of "1+1" patterns in optics, involving one space and one time dimension. Solitons and related phenomena, and their applications, are a superb example. The well-known analogy between dispersion and diffraction enables many of these results to be carried over into the spatial domain, with investigations of spatial solitons, both bright [6–8] and dark [9]. The natural extension into a second transverse dimension yields a "2+1" class of problems which have proved both rich and controversial, particularly in relation to "vortices" in lasers [10,11]. Driven dissipative systems have proved rewarding in this "2+1" domain, with predictions [12,13] and observations of hexagonal structures and turbulence in a variety of configurations, notably a Kerr-like medium with feedback mirror [14,15].

In this work we investigate a still bigger and harder problem, namely a "2+2" system, in which all three space dimensions as well as time are involved in the nonlinear interaction. We adopt the standard paraxial approximation, which is why we have a "2+2" rather than the ultimate "3+1" system. The configuration is conceptually very simple, and in essence extremely common in nonlinear optics, namely a slab of nonlinear medium in which optical fields counterpropagate. A seminal experiment using sodium vapor reported far-field hexagon structures [16]. More recently a similar configuration employing rubidium vapor with continuous-wave excitation displayed a rich spectrum of patterns, including hexagons (both near and far field) and rolls, as well as other less generic patterns [17].

Neither of these media is adequately described by a Kerr nonlinearity, but the phenomena we describe are much more dependent on the geometry than the particular form of the nonlinearity. Indeed Grynberg [18,19] and co-workers have themselves used a Kerr model to obtain qualitiative and even semiquantitative agreement with these experiments. On the other hand, pattern formation in Kerr media need not, and generally does not, exhibit the key features to be discussed below. For example *cross-phase modulation* and *standing-wave effects*, which are essential to the formation of square patterns, are absent in recent experiments in liquid-crystal light valve systems [20,21] which exhibit a large quasi-Kerr nonlinearity, and are in fact examples of "2+1" systems as are Refs. [14,15].

In parallel with the atomic vapor experiments, theoretical and computer investigations of systems of this type [18,19,22–25] lent credence to the hypothesis that these patterns could be ascribed to self- and cross-phase modulations of the counterpropagating fields. Analytical results, *in the linear limit*, gave thresholds and characteristic length scales in acceptable agreement with the experiments, while simulations in both one [23] and two [24] transverse dimensions confirmed the linear analysis, and suggested that hexagonal patterns are indeed the natural formation, at least for self-focusing media.

In this work we report substantial extensions of these previous results, particularly in the regime of self-defocusing Kerr media. We are able to demonstrate by nonlinear perturbation analysis that two very different pattern-forming modes exist, indeed coexist, in this system. One is a fairly conventional hexagon-forming mode and is dominant in self-focusing media. The other might be described as a roll-pattern mode, but we find that rolls are unstable. Instead square patterns emerge, and seem to be dominant for self-defocusing media where the medium supports short-period index gratings, and thus patterns with a well-defined and finite critical transverse wave vector [22]. By varying the grating parameter G (see below) one can favor one or other of these modes, but the influence of the less-favored mode makes itself felt quite close to the instability threshold, mediating defect formation and a Hopf bifurcation.

II. BASIC MODEL

We consider forward and backward amplitudes F and B in a Kerr medium of length L, as shown in Fig. 1. For simplicity we assume that the response is instantaneous and that the fields, and any instabilities, are scalar. Including the vector nature of the fields or the material response leads to plane-wave instabilities [26,27], a complication we want to avoid. Furthermore, the Kerr slab is assumed to have perfect antireflection coatings since otherwise cavity instabilities [28] may be present.

With these assumptions in mind the following equations are obtained:

$$\frac{\partial F}{\partial z}+\frac{\partial F}{\partial t}=i\beta\nabla^2F+iD(|F|^2+G|B|^2)F,$$
$$-\frac{\partial B}{\partial z}+\frac{\partial B}{\partial t}=i\beta\nabla^2B+iD(G|F|^2+|B|^2)B. \tag{2.1}$$

We have scaled z to the slab thickness L and t to the transit time n_0L/c. The diffraction parameter β is $L\lambda/4\pi$ in "real" units, where λ is the optical wavelength, and the Laplacian is in the transverse coordinates x, y only, establishing the "2+2" nature of the problem. The stress parameter D scales Kerr effect, slab thickness, and field amplitude into a single nonlinearity parameter, such that a single field of unit amplitude experiences a self-phase shift of D radians in traversing the slab. The remaining parameter, G, relates the self- and cross-phase modulations. Physically, G values between 2, 1, and (trivially) 0 are of interest [23], but all real values can be analyzed in a single framework.

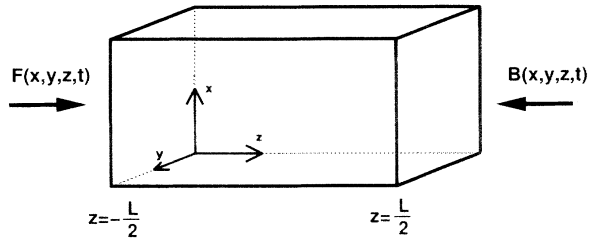

FIG. 1. Kerr medium and beam configuration.

Boundary conditions are all-important in this problem: we assume that the slab is irradiated from each side by *constant* input beams. Stability of any solution pair F, B is then a boundary value problem, not an eigenvalue problem: it requires that all solutions of the linearized equations consistent with the boundary conditions must be damped in *time*. This is in marked contrast to related propagation problems [29], where stability merely requires that all eigenvalues of the perturbation matrix have negative real parts.

These equations are derivable from a Lagrangian

$$L=\int\frac{i}{2}((FF_t^*-F^*F_t+BB_t^*-B^*B_t)+(FF_z^*-F^*F_z-BB_z^*+B^*B_z))$$
$$-\frac{D}{2}((1+G)(|F|^2+|B|^2)^2+(1-G)(|F|^2-|B|^2)^2)+\beta(|\nabla F|^2+|\nabla B|^2)\,d\mathbf{x}\,dz, \tag{2.2}$$

whose form strongly indicates that $G=1$ is a special case, and indeed the corresponding "1+1" problem is integrable for that case [30]. That "1+1" system is not integrable for other nonzero G values: we will be mainly concerned with such values. An immediate consequence of the manifest invariance of the Lagrangian under phase rotations of either F or B are the conservation laws

$$(\partial_t+\partial_z)\langle|F|^2\rangle=(\partial_t-\partial_z)\langle|B|^2\rangle=0. \tag{2.3}$$

Here the $\langle\ \rangle$ brackets denote either an integral or an average over transverse coordinates, while the derivatives are along the respective characteristics. It follows that input plane waves at $z=\pm1/2$ give rise to a simple zero-order homogeneous solution

$$F_0(z)=F_0(-\tfrac{1}{2})\exp\left(iD(1+G)(z+\tfrac{1}{2})\right),$$
$$B_0(z)=B_0(+\tfrac{1}{2})\exp\left(iD(1+G)(\tfrac{1}{2}-z)\right). \tag{2.4}$$

In the analysis and numerical investigations we adopt a scaling such that the input amplitude is unity and vary D, which is equivalent to varying the input intensity (or indeed the slab thickness or Kerr coefficient). Because of the conservation laws (2.3) and the absence of reflections, instability in this system arises through spatial redistribution of the optical energy as it traverses the slab due to cross- and self-phase modulation. This redistribution involves all three spatial dimensions in an essential way.

It is the linear, and nonlinear, stability of the homogeneous solution (2.4) which we are going to consider in the following sections. In order to do so we make a change of variables to a basis most convenient to display the structure and symmetries of the problem. We first set

$$F=F_0(1+f)\ ,\quad B=B_0(1+b) \tag{2.5}$$

along with the boundary conditions

$$f(z=-\tfrac{1}{2})=b(z=+\tfrac{1}{2})=0. \tag{2.6}$$

On replacing (2.5) into (2.1) we find the following coupled equations:

$$(\partial_t+\partial_z)f=i\beta\nabla^2f+iD((f+f^*+|f|^2)$$
$$+G(b+b^*+|b|^2))(1+f),$$
$$(\partial_t-\partial_z)b=i\beta\nabla^2b+iD(G(f+f^*+|f|^2)$$
$$+(b+b^*+|b|^2))(1+b). \tag{2.7}$$

This form displays the symmetries and physics of the problem but for analytical purposes we choose a different basis by reexpressing the four variables (f, f^*, b, b^*) in terms of a real column vector $\mathbf{U} \in \mathbb{R}^4 = [U_1, U_2, U_3, U_4]^t$:

$$f = \tfrac{1}{4}(U_1 + U_3 + i(U_2 + U_4));$$
$$b = \tfrac{1}{4}(U_3 - U_1 + i(U_2 - U_4)). \tag{2.8}$$

We will use the notation that $\mathbf{V} \in \mathbb{R}^2 = [U_1, U_2]^t$ and $\mathbf{W} \in \mathbb{R}^2 = [U_3, U_4]^t$. Using (2.8) in (2.7) leads to the compact form

$$J\partial_t \mathbf{U} + \mathcal{L}\mathbf{U} = D\mathcal{N}_1(\mathbf{U}|\mathbf{U}) + D\mathcal{N}_2(\mathbf{U}|\mathbf{U}|\mathbf{U}), \tag{2.9}$$

with boundary conditions given by

$$\mathbf{V}(\mathbf{x}, z = -\tfrac{1}{2}) + \mathbf{W}(\mathbf{x}, z = -\tfrac{1}{2}) = \mathbf{0},$$
$$\mathbf{W}(\mathbf{x}, z = \tfrac{1}{2}) - \mathbf{V}(\mathbf{x}, z = \tfrac{1}{2}) = \mathbf{0}. \tag{2.10}$$

The detailed form of the operators in (2.9) are shown in Appendix A. The linear operator $\mathcal{L} = \partial_z - M$, M being a matrix which depends on ∇^2, D, and G. The nonlinear operators are of the order indicated by their arguments, i.e., $\mathcal{N}_1$ is quadratic while $\mathcal{N}_2$ is cubic. Equation (2.9) will be the starting point for our analysis.

III. LINEAR ANALYSIS

In this section we will review the linear stability analysis of (2.9), and present results which turn out to play an important role in deciding which patterns our nonlinear system may select. In Sec. III A we will calculate the explicit form of the linear solutions, and derive the equation which defines when such solutions exist. This is done exclusively for the case of equal pump intensities, since we can take advantage of the consequent reflection symmetry to obtain fairly simple exact solutions. We do not expect these results to change dramatically for the case of slightly unequal pump intensities provided we operate close to the instability threshold. In Sec. III B we review the form of the neutral stability curves, which come in two groups, and present the explicit form of the linear solution on each of these curves. Furthermore we show that the analysis for negative values of the grating parameter G presents no new difficulties and gives insight into the structure and symmetry of the problem. In Sec. III C we demonstrate that one group of threshold curves defines a linear solution which has an even symmetry in z, while the other group of curves defines a linear solution that has an odd symmetry in z. Since the symmetry of the linear solution is important in terms of pattern selection, we show in Sec. III D that the first mode to become unstable for $DG > 0$ is an even mode, while an odd mode first becomes unstable for $DG < 0$, provided the spatial grating is present ($G > 1$). In Sec. III E we compute the adjoint solutions of the linear problem, as we will need those to carry out a nonlinear analysis.

A. Linear equations

It has previously been shown [23] that, in most parameter regimes, the equilibrium plane-wave state becomes unstable, on increasing $|D|$, to a transverse perturbation with finite wave number, a precursor for pattern formation. The resulting instability is stationary in the sense that its temporal frequency is zero. For self-focusing media ($D > 0$), all values of G ($G \neq 0$) result in such an instability. For self-defocusing media ($D < 0$), however, there is a set of G for which the equilibrium solution first becomes unstable to a short-wavelength perturbation, which actually coincides with the phase-conjugate oscillation (PCO) limit [23] of this system. We will only consider values of G for which this is not the case.

The linearized equations are obtained by dropping all nonlinear terms in (2.9) to give

$$J\partial_t \mathbf{U} + \mathcal{L}\mathbf{U} = \mathbf{0}. \tag{3.1}$$

We look for solutions of the form

$$\mathbf{U}(\mathbf{x}, z, t) = \mathbf{u}(z) e^{i\mathbf{k}\cdot\mathbf{x} + \lambda t}, \quad \lambda = \sigma + i\omega, \tag{3.2}$$

which must satisfy the boundary conditions

$$\mathbf{v}(z = -\tfrac{1}{2}) + \mathbf{w}(z = -\tfrac{1}{2}) = \mathbf{0},$$
$$\mathbf{w}(z = \tfrac{1}{2}) - \mathbf{v}(z = \tfrac{1}{2}) = \mathbf{0}. \tag{3.3}$$

Several authors have previously analyzed this problem in great detail [22,23,25,31–33]. The threshold for instability of the homogeneous solution (2.4) is obtained by setting $\sigma = 0$. When the input beams are of equal intensity, the lowest threshold for instability corresponds to a static instability where $\omega = 0$. The instability may become oscillatory when the pumps are of unequal intensity, and we refer the reader to previous publications [25,32,33], detailing the resulting linear analysis, for this case. Here we only consider the case of equal pump intensities. In this regime we may set $\omega = 0$, in which case the linear equations (3.1) decouple into the form

$$\partial_z \mathbf{u}(z) = M\mathbf{u}(z), \quad M = \begin{bmatrix} M_1 & 0 \\ 0 & M_2 \end{bmatrix}, \quad M_j = \begin{bmatrix} 0 & \beta k^2 \\ -\psi_j^2/\beta k^2 & 0 \end{bmatrix}, \quad j = 1, 2, \tag{3.4}$$

where $\psi_1^2 = \beta k^2(\beta k^2 + 2D(G-1))$ and $\psi_2^2 = \beta k^2(\beta k^2 - 2D(G+1))$. Notice that ψ_1 or ψ_2 may be imaginary. Solutions to this system are of the form

$$\mathbf{u}(z) = \exp(M(z + \tfrac{1}{2}))\mathbf{u}(-\tfrac{1}{2}) = \begin{bmatrix} \exp(M_1(z + \frac{1}{2})) & 0 \\ 0 & \exp(M_2(z + \frac{1}{2})) \end{bmatrix} \mathbf{u}(-\tfrac{1}{2}), \tag{3.5}$$

where the off-diagonal nature of M_j makes explicit exponentiation straightforward (see Appendix B):

$$\exp(M_j z) = \begin{bmatrix} \cos(\psi_j z) & \frac{\beta k^2}{\psi_j}\sin(\psi_j z) \\ -\frac{\psi_j}{\beta k^2}\sin(\psi_j z) & \cos(\psi_j z) \end{bmatrix}. \quad (3.6)$$

On applying the boundary conditions we find that

$$(\exp(M_1) + \exp(M_2))\mathbf{v}(-\tfrac{1}{2}) = \mathbf{0}. \quad (3.7)$$

Nontrivial solutions exist when $\det(\exp(M_1) + \exp(M_2)) = 0$. From Eq. (3.6) this condition is given by

$$2 + 2\cos(\psi_1)\cos(\psi_2) + \left(\frac{\psi_1}{\psi_2} + \frac{\psi_2}{\psi_1}\right)\sin(\psi_1)\sin(\psi_2) = 0, \quad (3.8)$$

which agrees with previous analysis of this system [23].

B. Threshold curves

The threshold curves for onset of stationary instability are given by the solutions of (3.8). To generate neutral stability curves in the βk^2-D plane we choose a value of k^2 and find the value of D which solves Eq. (3.8) for a given value of G. Due to the transcendental nature of (3.8) we find that there are an infinite number of neutral stability curves. These curves, however, split into two groups because (3.8) may be factorized to give

$$H_1\, H_2 = 0, \quad (3.9)$$

where the function H_1 is defined by

$$H_1(\psi_1^2, \psi_2^2) = \frac{\psi_1}{\psi_2}\sin(\psi_1/2)\sin(\psi_2/2) + \cos(\psi_1/2)\cos(\psi_2/2) \quad (3.10)$$

and $H_2(\psi_1^2, \psi_2^2) = H_1(\psi_2^2, \psi_1^2)$. A group of threshold curves are defined by $H_1 = 0$ with the other group of curves defined by $H_2 = 0$, and they cross when $H_1 = H_2 = 0$. In Fig. 2 we plot against βk^2 the lowest value of $|D|$ for which $H_1 = 0$ and the lowest value of $|D|$ for which $H_2 = 0$, for the key cases of $G = 1, 2$. The threshold diverges as $k \to 0$, while for large k we find that $|DG| \to \pi/2$, which is equivalent to the standard PCO limit.

As $|D|$ is increased, the system becomes unstable on crossing the lowest curve. Instability will therefore occur at the k value that has the lowest value of $|D|$. We denote this point in the βk^2-D plane as the critical point and label it $(\beta k_c^2, D_c)$. Note that in three of the four cases illustrated this value of k_c corresponds to that of the minimum threshold intensity. In the fourth case $(D < 0, G = 1)$ the lowest threshold occurs in the large-k domain, and is exactly the PCO limit. As mentioned earlier this case, and any like it, will not be considered further.

One of the reasons for considering $G \in \mathbb{R}$ is that the analysis for negative G presents no new difficulties. In fact the results are almost identical and yet the differences are very important. Notice that $G \to -G \Rightarrow \psi_1^2 \to \psi_2^2$. Since $\psi_1^2 \to \psi_2^2 \Rightarrow H_1 \to H_2$ the threshold curves are identical, except that any curve defined by $H_1 = 0$ for positive G will be defined by $H_2 = 0$ for negative G, and vice versa.

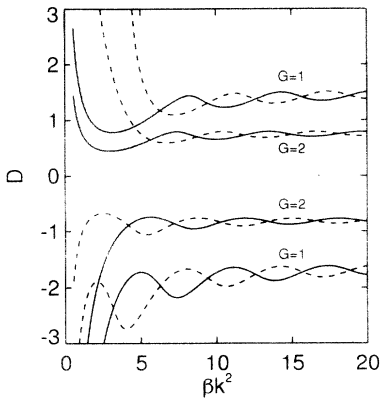

FIG. 2. Threshold intensity for focusing ($D > 0$) and defocusing media ($D < 0$). The solid lines represent neutral curves defined by $H_2 = 0$ while the dashed lines represent those defined by $H_1 = 0$.

The crossing points occur when $H_1 = H_2 = 0$. The difference, $H_1 - H_2$, is given by

$$H_1 - H_2 = \left(\frac{\psi_1}{\psi_2} - \frac{\psi_2}{\psi_1}\right)\sin(\psi_1/2)\sin(\psi_2/2) = \frac{4DG\beta k^2}{\psi_1\psi_2}\sin(\psi_1/2)\sin(\psi_2/2). \quad (3.11)$$

In general then $H_1 = H_2$ when one or both of the sine terms vanish. This happens if $\psi_i = 2m\pi, m = 1, 2, \ldots$ and when this is the case

$$H_1 = H_2 = \cos(\psi_1/2)\cos(\psi_2/2). \quad (3.12)$$

If $\psi_i = \pi$ then $H_1 = H_2 = 0$ requires that $\psi_j = (2n+1)\pi$, $i \neq j, n = 0, 1, 2, \ldots$. Hence the crossing points are given when both ψ_1 and ψ_2 are integer multiples of π, say $m\pi$, $n\pi$ where one of the m, n must be even, the other odd. If $DG > 0$ then $m > n$ and $m < n$ if $DG < 0$. The location of the (m, n) crossing point in the βk^2-D plane is given by $(m > n > 0)$,

$$|D| = \frac{(m^2 - n^2)\pi^2}{4\beta k^2 |G|}, \qquad (\beta k^2)^2 = \frac{\pi^2}{2}\left(m^2 + n^2 + \mathrm{sgn}(D)\frac{(m^2 - n^2)}{|G|}\right). \quad (3.13)$$

A little calculation shows that $|D|$ is smallest for $m = n+1$, larger differences giving higher-order modes. These formulas are very useful for checking the threshold curves generated by (3.8).

We now have all the ingredients to write down the

linear solution at threshold. In particular we will be interested in the linear solution at $(\beta k_c^2, D_c)$. Away from the crossing points the solutions of (3.7) are given by

$$\mathbf{v}(-\tfrac{1}{2}) = \begin{bmatrix} -\beta k^2 \left(\dfrac{\sin\psi_1}{\psi_1} + \dfrac{\sin\psi_2}{\psi_2} \right) \\ \cos(\psi_1) + \cos(\psi_2) \end{bmatrix}. \tag{3.14}$$

This one-parameter family of solutions constitutes the null-space (N) of $(\exp(M_1)) + \exp(M_2)$ and consequently N is one-dimensional. Using (3.14) the linear solutions are given by (3.5) and the solutions in terms of the original basis can be constructed through (2.8). These solutions are defined at all points in the βk^2-D plane which lie on a threshold curve. Determination of the linear solution at the critical point requires that we know where the critical point is. Except for a few special cases we have to compute this point numerically. We can, however, say something in general about the symmetry of the linear solutions on the neutral stability curves.

C. Symmetry of linear solutions

The counterpropagating system (2.1) is invariant with respect to reflections about the midplane $z = 0$. This means that the linearized version of (2.7) is invariant under exchange of f and b while reflecting about the midplane. This symmetry, although noted earlier [19], has not been taken advantage of in previous analyses. As we pointed out earlier, away from the crossing points $\dim[N(\exp(M_1) + \exp(M_2))] = 1$, which allows us to conclude that

$$f(\mathbf{x}, z) = \rho b(\mathbf{x}, -z) \ , \ b(\mathbf{x}, z) = \rho f(\mathbf{x}, -z). \tag{3.15}$$

On applying this symmetry one more time we see that $\rho = \pm 1$. In terms of our new basis this symmetry takes the form

$$\mathbf{u}(z) = \rho P \mathbf{u}(-z) \ , \ P = \begin{bmatrix} Q & 0 \\ 0 & -Q \end{bmatrix} \ , \ Q = \begin{bmatrix} -1 & 0 \\ 0 & 1 \end{bmatrix}. \tag{3.16}$$

The possibility of having two values of ρ, combined with the result that the threshold curves are defined by one of two factors being zero, suggests that the value of ρ may depend on which neutral curve we are on. Indeed this is the case, and we have proved the following result (see Appendix B):

$$\begin{aligned} &\text{If } H_1 = 0 \text{ and } H_2 \neq 0 \text{ then } \rho = -1; \\ &\text{If } H_2 = 0 \text{ and } H_1 \neq 0 \text{ then } \rho = +1. \end{aligned} \tag{3.17}$$

Therefore the linear solutions have even symmetry ($\rho = +1$) when we cross a curve defined by $H_2 = 0$ while they have odd symmetry ($\rho = -1$) when we cross a curve defined by $H_1 = 0$.

D. First curve crossed

We have been able to show that the linear solutions at threshold can be characterized by a symmetry involving the exchange of the counterpropagating fields. On one set of curves $f(\mathbf{x}, z) = b(\mathbf{x}, -z)$ while on the other set $f(\mathbf{x}, z) = -b(\mathbf{x}, -z)$. As we increase our stress parameter the system first becomes unstable at $(\beta k_c^2, D_c)$. If we know which curve this point lies on then we immediately know about the symmetry of the linear solutions at the onset of instability. It is therefore of interest to calculate which curve we cross first. We have been able to prove the following result for $G \notin [-1, 1]$ (see Appendix B):

$$\begin{aligned} &\text{If } DG > 0 \text{ then } H_2 \to 0 \text{ first;} \\ &\text{If } DG < 0 \text{ then } H_1 \to 0 \text{ first.} \end{aligned} \tag{3.18}$$

Thus the even mode gives the first minimum (i.e., the one closest the optical axis k = 0) for $DG > 0$, and the odd mode for $DG < 0$. Since in most cases this is also the mode with the lowest threshold D, this has profound consequences for the nonlinear behavior and the pattern formation, as we will see in the following section.

E. Adjoint solutions

Before proceeding to consider the nonlinear stability of (2.4) we calculate the adjoint solutions of (3.1), since we will need these in the following section. If we define the adjoint problem in the usual manner [34],

$$\langle \mathcal{L}\mathbf{u}, \mathbf{u}^A \rangle = \langle \mathbf{u}, \mathcal{L}^A \mathbf{u}^A \rangle, \tag{3.19}$$

then integration by parts shows that $\mathbf{u}^A$ must satisfy

$$\mathcal{L}^A \mathbf{u}^A = (\partial_z + M^t)\mathbf{u}^A = \mathbf{0}, \tag{3.20}$$

along with the adjoint boundary conditions

$$\begin{aligned} &\begin{pmatrix} u_1^A \\ u_2^A \end{pmatrix}(1/2) + \begin{pmatrix} u_3^A \\ u_4^A \end{pmatrix}(1/2) = \mathbf{0} \ , \\ &\begin{pmatrix} u_1^A \\ u_2^A \end{pmatrix}(-1/2) - \begin{pmatrix} u_3^A \\ u_4^A \end{pmatrix}(-1/2) = \mathbf{0}. \end{aligned} \tag{3.21}$$

Again the solution to (3.20) can be explicitly calculated, and indeed a little algebra reveals that it is possible to write the adjoint in terms of the linear solutions through

$$\mathbf{u}^A(z) = \begin{bmatrix} \mathcal{K} & 0 \\ 0 & \mathcal{K} \end{bmatrix} \mathbf{u}(-z) \ , \ \mathcal{K} = \begin{bmatrix} 0 & 1 \\ 1 & 0 \end{bmatrix}. \tag{3.22}$$

IV. NONLINEAR ANALYSIS

In this section we present the results and details of a nonlinear analysis of the full counterpropagation equa-

tions. A previous nonlinear analysis of this system [19] removed the longitudinal structure by taking, what essentially amounts to, a mean-field limit. This limit, however, forces hexagonal structures since it assumes that the linear solution is an even mode. The relevance of this last comment will become clear. In Sec. IV A we present the technical background required to carry out a "weakly nonlinear" analysis, both for completeness and for the reader not versed in these techniques. Having done so we first apply these techniques in one transverse dimension, both to demonstrate the solution process and to show that excellent agreement between numerical and analytical results can be obtained. This is detailed in Sec. IV B. Finally, we analyze in Sec. IV C pattern formation in two transverse dimensions. In particular we show that in self-focusing media the quadratic nonlinearity that is responsible for hexagonal pattern formation is large and makes hexagons the likely pattern, as we demonstrate by numerical simulation in the following section. Furthermore, we show that in self-defocusing media the quadratic term vanishes, as a direct consequence of the symmetry of the linear mode. Further analysis points to the likelihood of square patterns which saturate at quintic order rather than the usual cubic order, another prediction that we have confirmed through numerical simulation. Our analysis reveals many subtleties and complexities involved in this problem which we have only partially resolved. These features may interest the patterns community in general.

A. Theory

In the preceding section we saw that there is a critical value of D, above which the homogeneous plane-wave solution (2.4) becomes unstable to perturbations at a finite wave number. Of course, due to the rotational degeneracy of the problem, there are a continuum of such modes and in two transverse dimensions these lie on a circle of radius k_c. From a linear point of view all of these modes are equally favored and the final outcome is determined by nonlinear coupling between these modes. In many physical systems the resulting dynamics is limited to one (rolls), two (rhombi), or three (hexagons) modes. The goal of this section is to investigate which configuration is preferred for our system.

Our analysis is restricted to considering the possible patterns near onset where

$$D = D_c(1+\epsilon); \quad \epsilon \ll 1, \tag{4.1}$$

and we proceed by expanding the field $\mathbf{U}$ in an asymptotic series depending on the stress parameter ϵ,

$$\mathbf{U}(\mathbf{x}, z, t) = \sum_{n=0}^{\infty} \mu_n(\epsilon)\mathbf{U}^{(n)}(\mathbf{x}, z, t), \tag{4.2}$$

where the members of the series are determined by the nonlinear balances and $\mu_0(\epsilon)$ is chosen to balance the linear growth rate with the leading nonlinear correction. The zeroth-order solution $\mathbf{U}^{(0)}$ is taken to be a linear combination of the Fourier modes which lie on the critical circle, each with their own amplitude A_j

$$\mathbf{U}^{(0)} = \mathbf{u}^{(0)}(z)\left(\sum_{j=1}^{N} A_j e^{i\mathbf{k}_j\cdot\mathbf{x}} + \text{c.c.}\right); \quad |\mathbf{k}_j| = k_c, \tag{4.3}$$

where $\mathbf{u}^{(0)}(z)$, which depends on k, is the longitudinal structure of the neutrally stable mode. To make allowance for the slow temporal dynamics of these modes we allow their amplitudes to depend on multiple time scales so that

$$\partial_t = \epsilon\partial_{T_1} + \epsilon^2\partial_{T_2} + \cdots . \tag{4.4}$$

Figure 2 indicates that above threshold there exists a finite bandwidth of modes which become unstable. We may include this sideband degeneracy effect by allowing the A_j's to depend on slow spatial scales X and Y but we pay the price in that the dynamics of the A_j's are described by partial differential equations. The advantage is that not only do we correctly capture the behavior near D_c, but the partial differential equations that the A_j 's satisfy are universal, and are often referred to as the *order parameter equations* [2]. At this point we are primarily interested in the existence of certain patterns and so we may ignore the finite bandwidth effect, derive a set of ordinary differential equations for the A_j's, and determine which patterns are likely. If necessary we can then add the envelope structure which allows for transverse modulations of the amplitudes.

Replacing (4.1), (4.2), and (4.4) into (2.9) gives rise to a set of equations at each order in ϵ. For a given value of ϵ, equations for the amplitudes A_j are obtained as solvability conditions which must be applied in order to compute the iterates $\mathbf{U}^{(1)}, \mathbf{U}^{(2)}, \ldots$ in the expansion (4.2). When the solvability conditions up to third order are combined (this is the first order with saturation) we arrive at amplitude equations which assume the generic form

$$\partial_t A_j = \epsilon A_j + \sigma_{jlm} A_l^* A_m^* - \sum_{l=1}^{N} \gamma_{jl} A_l A_l^* A_j \ ; \qquad j = 1, \ldots, N \tag{4.5}$$

and have been derived by many authors in a multitude of physical contexts. The quadratic coefficient σ_{jlm} can only be nonzero when $\mathbf{k}_j + \mathbf{k}_l + \mathbf{k}_m = \mathbf{0}$ ($N = 3$). In rotationally degenerate problems (where the critical modes lie on a circle) this condition may only be satisfied when each of the three wave vectors mutually subtend an angle of $2\pi/3$, thus forming an hexagonal pattern. If σ_{jlm} is nonzero we know that, sufficiently close to threshold, the quadratic term will initially dominate, leading to hexagonal patterns. However, since there is no saturation at this order, we cannot say, in general, what the long term behavior of the system is. Experience [1] leads us to expect that hexagonal patterns of transcritical type will dominate. This situation is generic in the absence of further structure or symmetry. However, a symmetry such as the inversion symmetry $A_i \to -A_i$ may force $\sigma_{jlm} \equiv 0$.

The cubic terms are generically present, with or without the inversion symmetry, and arise from interactions which involve three-wave mixing of the form $\mathbf{k}_j + \mathbf{k}_l - \mathbf{k}_l$.

If the quadratic coefficient is $O(\epsilon^{1/2})$ then we may balance linear, quadratic, and cubic terms by choosing A_j also to be $O(\epsilon^{1/2})$. In this case the behavior is captured by the bifurcation diagram [35] shown in Fig. 3. For $\epsilon_1 < \epsilon < \epsilon_3, \epsilon_1 < 0$, hexagons are stable while for $\epsilon > \epsilon_2$, rolls are stable. In between, $\epsilon_2 < \epsilon < \epsilon_3$, the two states may coexist although one may invade the other.

If, on the other hand, the coefficient σ_{jlm} is $O(1)$ then the subcritical solution which balances linear and quadratic terms is unstable and there are no small amplitude stable solutions. Nothing can rigorously be said about the final outcome, although in many problems the hexagonal branch will turn around and become the stable solution. It appears that a hexagonal pattern is generically preferred [1] close to threshold unless the inversion symmetry $A_i \to -A_i$ is present, although we know of no concrete results concerning this.

Before we consider hexagons in more detail, we first look at the case of rolls ($N = 1$). The reason for this is twofold. Since this calculation only involves one mode the algebra is not too involved and we may step through it in order to highlight certain parts of the solution process. For hexagons and rhombi we will not show the details, only the final result. Furthermore, the only relevant "pattern" in one tranverse dimension is the roll and we will be able to show excellent agreement between analysis and numerics in this case.

B. One transverse dimension

In one tranverse dimension, the null space of $\mathcal{L}$ is one-dimensional, so we choose the zeroth-order solution $\mathbf{U}^{(0)}$ to be of the form

$$\mathbf{U}^{(0)}(x,z) = \mathbf{u}^{(0)}(z;k_c)(Ae^{ik_c x} + \text{c.c.}), \tag{4.6}$$

where the roll amplitude A is determined by a nonlinear balance between linear and cubic terms. To capture this balance we choose $\mu_0(\epsilon) = \epsilon^{1/2}$, $\mu_1(\epsilon) = \epsilon$, $\mu_2(\epsilon) = \epsilon^{3/2}$, and so forth. We expand the operators in (2.10) in terms of ϵ (see Appendix C) and group the resulting terms at each order in ϵ. At first order we recover the linear problem

$$O(\epsilon^{1/2}): \quad \mathcal{L}^{(0)}(\nabla^2)\mathbf{U}^{(0)} = (\partial_z - M(\nabla^2))\mathbf{U}^{(0)} = \mathbf{0}, \tag{4.7}$$

which has the solution given in (4.6). At next order we have

$$O(\epsilon): \quad \mathcal{L}^{(0)}(\nabla^2)\mathbf{U}^{(1)} = D_c\mathcal{N}_1(\mathbf{U}^{(0)}|\mathbf{U}^{(0)}) = D_c\mathcal{N}_1(\mathbf{u}^{(0)}|\mathbf{u}^{(0)})(Ae^{ik_c x} + \text{c.c.})^2 \tag{4.8}$$

and the source terms on the right hand side generate new Fourier components at both k=0 and k=$2k_c$. We therefore seek a solution of the form

$$\mathbf{U}^{(1)}(x,z) = \mathbf{u}^{(1)}(z;k=0)(|A|^2 + \text{c.c.}) + \mathbf{u}^{(1)}(z;k=2k_c)(A^2e^{2ik_c x} + \text{c.c.}) \tag{4.9}$$

and for each Fourier component $\mathbf{u}^{(1)}(z;k)$ we obtain the nonhomogeneous boundary value problem

$$\mathcal{L}^{(0)}(k)\,\mathbf{u}^{(1)}(z;k) = \mathcal{R}(z), \tag{4.10}$$

where the operators are defined by

$$\mathcal{L}^{(0)}(k) = \partial_z - M(k)\ , \qquad \mathcal{R}(z) = D_c\mathcal{N}_1(\mathbf{u}^{(0)}(z;k_c)|\mathbf{u}^{(0)}(z;k_c)). \tag{4.11}$$

The vector $\mathbf{u}^{(1)}(z;k)$ must satisfy the same boundary conditions as the linear eigenvector (3.3). The solution of (4.11) can formally be written as

$$\mathbf{u}^{(1)}(z;k) = \int_{-1/2}^{z} \exp\left(M(k)(z-z')\right)\mathcal{R}(z)\,dz' + \exp\left(M(k)(z+1/2)\right)\mathbf{u}^{(1)}(-1/2;k). \tag{4.12}$$

If we define the indefinite integral in (4.12) to be $\mathcal{J}(z;k) \in \mathbb{R}^4 = [\mathcal{J}_1, \mathcal{J}_2, \mathcal{J}_3, \mathcal{J}_4]^t$ then the boundary term, $\mathbf{u}^{(1)}(-1/2;k)$, is given by the solution of

$$(e^{M_1} + e^{M_2}) \begin{pmatrix} u_1^{(1)} \\ u_2^{(1)} \end{pmatrix} (-1/2;k) = \begin{pmatrix} \mathcal{J}_3 \\ \mathcal{J}_4 \end{pmatrix} (1/2;k) - \begin{pmatrix} \mathcal{J}_1 \\ \mathcal{J}_2 \end{pmatrix} (1/2;k). \tag{4.13}$$

The operator on the left hand side is the linear operator of Eq. (3.7) which becomes singular for $k = k_c$. For $k \neq k_c$ we can invert it and obtain the boundary term $\mathbf{u}^{(1)}(-1/2;k)$. Thus we have completely determined $\mathbf{u}^{(1)}(z;k)$ which gives us the solution at $O(\epsilon)$ through (4.12). Although we can write down the formal solution, including the exponential in (4.12), there are many

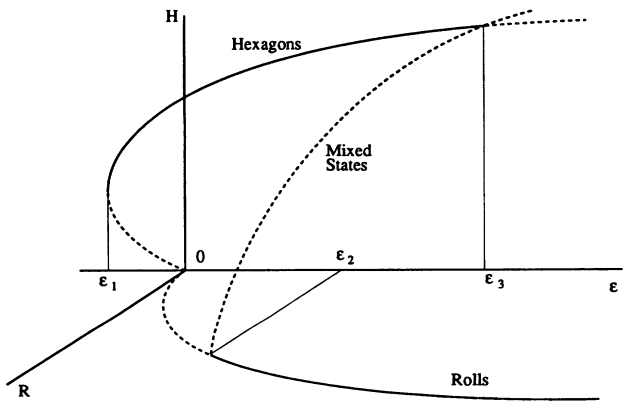

FIG. 3. Amplitude of the hexagon state (H) and the roll state (R) as a function of the stress parameter ϵ. Solid lines denote stable states, dashed lines unstable states.

details involved and in general we calculate $\mathbf{u}^{(1)}(z;k)$ numerically. Having solved at $O(\epsilon)$ we now proceed to third order, where the equations read

$$O(\epsilon^{3/2}):$$

$$J\partial_{T_1}\mathbf{U}^{(0)}+\mathcal{L}^{(0)}\mathbf{U}^{(2)} = \mathcal{L}^{(1)}\mathbf{U}^{(0)} + D_c(\mathcal{N}_1(\mathbf{U}^{(0)}|\mathbf{U}^{(1)}) + \mathcal{N}_1(\mathbf{U}^{(1)}|\mathbf{U}^{(0)})) + D_c\mathcal{N}_2(\mathbf{U}^{(0)}|\mathbf{U}^{(0)}|\mathbf{U}^{(0)}). \quad (4.14)$$

At this order we generate source terms at $k = k_c$ and $k = 3k_c$. In order to maintain an asymptotic expansion which is uniformly bounded in space, the Fredholm alternative [34] requires that the projection of the source terms on the null space of the adjoint $\mathcal{L}^A$ must be zero. The only terms that may have nonzero projection are those with critical wave number $k = k_c$. There are both linear (in A) and nonlinear (cubic) source terms at $k = k_c$. The linear terms arise from $J\partial_{T_1}\mathbf{U}^{(0)}$ and $\mathcal{L}^{(1)}\mathbf{U}^{(0)}$ while the cubic terms arise from both $\mathcal{N}_1$ and $\mathcal{N}_2$. Projecting these terms against the adjoint, $\mathbf{v}(z)$, leads to the result

$$\tau_0\partial_{T_1}A = A - \gamma|A|^2A \quad (4.15)$$

and, on returning to unscaled units, we obtain the amplitude equation

$$\tau_0\partial_t A = \epsilon A - \gamma|A|^2A. \quad (4.16)$$

If $\gamma > 0$ there is a stable solution of Eq. (4.16), with amplitude given by $A = \sqrt{\epsilon/\gamma}$. In one transverse dimension these rolls are the only possible solution and in Fig. 4 we plot the amplitude A obtained from (4.16) along with the results of numerical simulations on the full system (2.1). We only show the result for a defocusing medium with $G = +2$, but the agreement is also excellent for other values of G in both focusing and defocusing media.

C. Two transverse dimensions

We will now consider pattern formation in two transverse dimensions, where we must examine the stability of the roll solution to other patterns, such as rhombi or hexagons. Since transcritical hexagons are expected to dominate, we first determine when they are possible. In order to do so, we make use of our results concerning the symmetry of the linear solutions to prove, in a very simple manner, that the odd mode ($f(\mathbf{x},z) = -b(\mathbf{x},-z)$) has the inversion symmetry $A_j \to -A_j$. As a result $\sigma \equiv 0$ and transcritical hexagons are not possible if the odd mode is the most unstable.

In the original basis the linear solutions take the form

$$\begin{bmatrix} f(\mathbf{x},z) \\ b(\mathbf{x},z) \end{bmatrix} = \begin{bmatrix} f_0(z) \\ b_0(z) \end{bmatrix} \left(\sum_j A_j e^{i\mathbf{k}_j\cdot\mathbf{x}} + \text{c.c.} \right) \quad (4.17)$$

and the amplitudes A_j obey

$$\partial_t A_j = \epsilon A_j + \sigma A_l^* A_m^* + \cdots . \quad (4.18)$$

Since our linear equations are invariant under reflections about the midplane then $[b(\mathbf{x},-z), f(\mathbf{x},-z)]^t$ is also a solution to the linear problem. We know that $f(\mathbf{x},z) = \rho b(\mathbf{x},-z)$ and hence the A_j's must also obey

$$\partial_t A_j = \epsilon A_j + \rho\sigma A_l^* A_m^* + \cdots . \quad (4.19)$$

As a consequence $\sigma \equiv 0$ when the most unstable mode is odd, since $\rho = -1$ in this case. As mentioned earlier, this is true for $DG < 0$ and for a self-defocusing medium ($D < 0, G > 0$) the odd mode has the lowest threshold for $G > 1.3$. We are lead to the conclusion that transcritical hexagons are not possible in this regime, and we will consider the possibility of rhombic patterns shortly.

For self-focusing media, where the most unstable mode is even, there is no inversion symmetry and, as shown in Fig. 5, $\sigma \neq 0$. Further inspection of Fig. 5 reveals that σ is $O(1)$ for all G. As we mentioned earlier, this means we may not simultaneously balance linear, quadratic, and cubic terms and we can say nothing further about hexagons, except that we expect them to be the stable solutions close to threshold, an expectation which is borne out by the numerics, as will be shown in the following section.

We now address the question of pattern formation in a self-defocusing medium, where we know, from the discussion above, that transcritical hexagons are not possible. If we consider solutions which consist of a superposition of N sets of rolls at various orientations then the following equations result:

$$\tau_0\partial_t A_i = \epsilon A_i - \sum_{j=1}^{N}\gamma_{ij}|A_j|^2A_i \ , \quad i = 1,\ldots,N, \quad (4.20)$$

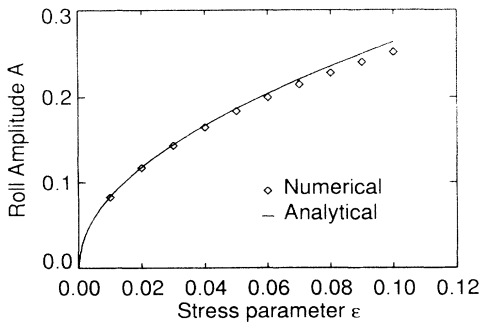

FIG. 4. Roll amplitude for a self-defocusing medium ($D < 0$) with $G = 2$. The numerical curve is obtained by simulation in one transverse dimension.

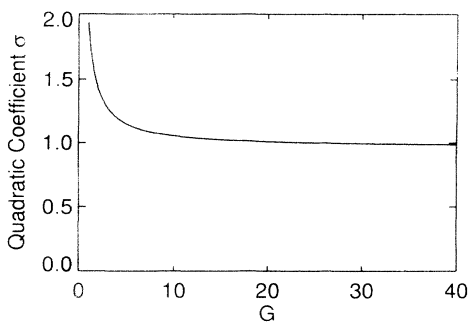

FIG. 5. The quadratic coefficient σ for a self-focusing medium ($D > 0$).

where the constants γ_{ij} depend on the angle between the modes $\mathbf{k}_i \cdot \mathbf{k}_j = \cos\theta_{ij}$. If chiral symmetry holds ($\theta \to -\theta$) the cubic coefficients are symmetric, i.e., $\gamma_{ij} = \gamma_{ji}$. A remarkable property of (4.20) is that it is a gradient system in the form

$$\tau_0 \partial_t A_i = -\frac{\delta \mathcal{F}}{\delta A_i^*}, \tag{4.21}$$

with the potential function $\mathcal{F}(A_1, ..., A_N, A_1^*, ..., A_N^*)$ given by

$$\mathcal{F} = -\epsilon \sum_{i=1}^{N} |A_i|^2 + \frac{1}{2} \sum_{i=1}^{N} \sum_{j=1}^{N} \gamma_{ij} |A_i|^2 |A_j|^2. \tag{4.22}$$

On differentiating (4.22) with respect to time it immediately becomes clear that

$$\partial_t \mathcal{F} = -2\tau_0 \sum_{i=1}^{N} |\partial_t A_i|^2 \leq 0 \tag{4.23}$$

and hence $\mathcal{F}$ is a Lyapunov function, implying that the dynamics of (4.20) will naturally move towards minima of $\mathcal{F}$. This is invaluable in deciding which configuration may be selected, especially if the matrix elements γ_{ij} can be computed explicitly.

Now consider the problem with two modes at angle θ. We can always scale the amplitudes such that $\gamma_{11} = \gamma_{22} = 1$, in which case

$$\begin{aligned} \tau_0 \partial_t A_1 &= \epsilon A_1 - (|A_1|^2 + \gamma(\theta)|A_2|^2) A_1, \\ \tau_0 \partial_t A_2 &= \epsilon A_2 - (|A_2|^2 + \gamma(\theta)|A_1|^2) A_2. \end{aligned} \tag{4.24}$$

This system has three types of fixed points given by the following.

(i) The plane-wave equilibrium state $A_j = 0, j = 1, 2$.
(ii) Roll solutions given by $A_1 = R\exp(i\phi_1)$, $A_2 = 0$ or $A_1 = 0$, $A_2 = R\exp(i\phi_2)$ with roll amplitude $R = \sqrt{\epsilon}$.
(iii) Rhombic solutions given by $A_1 = S\exp(i\phi_1)$, $A_2 = S\exp(i\phi_2)$ with amplitude $S = \sqrt{\epsilon/1 + \gamma(\theta)}$.

If $\epsilon < 0$ then the equilibrium solution is the only stable solution. For $\epsilon > 0$ we can compare the value of the Lyapunov function for rolls and rhombi:

$$\mathcal{F} \text{ (Rolls)} = -\epsilon^2/2, \text{ and } \mathcal{F} \text{ (Rhombi)} = -\epsilon^2/1 + \gamma(\theta).$$

There are essentially three regimes into which the dynamics may fall.

(i) If $\gamma(\theta) > 1$ for all θ, then rolls are stable with respect to rhombic perturbations.
(ii) If $\gamma(\theta) > -1$ for all θ, but $\gamma(\theta) < 1$ for some θ, then the θ which minimizes γ within this range will be preferred, as it has the lowest Lyapunov value.
(iii) Finally, if $\gamma(\theta) < -1$ for some θ then this configuration does not saturate at this order [solutions blow up in (4.24)]. To saturate the growth one should proceed to quintic order, and one would expect that it will again be the θ which minimizes γ that prevails at that order.

Following the procedures outlined in the calculation for rolls, we have computed the two mode amplitude equations for our system. The only significant difference is the appearance of new source terms at second order with wave number $k^2 = 2k_c^2(1 \pm \cos\theta)$ which present no added complications to the solution process. In Fig. 6 we show the value of the cubic coefficient γ as a function of the angle θ for the physically relevant case of a defocusing medium with $G = 2$. We immediately see that there is a finite band of θ, centered about $\pi/2$, for which $\gamma(\theta) < -1$. As mentioned above this implies that all patterns with angles in this range fail to saturate at cubic order. We expect the configuration which minimizes $\gamma(\theta)$ to dominate at quintic order. Note that $\pi/2$, which would correspond to a square, does not minimize $\gamma(\theta)$. However, the value of θ which does is very nearly $\pi/2$ and the difference is indetectable in our numerical simulations of (2.1).

The failure of the pattern to saturate at cubic order suggests that the equations should be expanded to quintic order—a rather formidable undertaking. We have not done this but we do observe squares numerically, and indeed they saturate at quintic order. The amplitude equation for a square pattern [$A_1 = S\exp(i\phi_1)$, $A_2 = S\exp(i\phi_2)$], to quintic order, is of the form

$$\partial_t S = \epsilon S + \gamma |S|^2 S - \delta |S|^4 S. \tag{4.25}$$

If $\gamma > 0$, $\delta > 0$ the homogeneous solution ($S = 0$) to (4.25) exhibits a subcritical bifurcation at $\epsilon = 0$ [36]. Subcritical solutions exist for $\epsilon \in [-\gamma^2/4\delta, 0]$. We have already calculated γ but, as mentioned above, we have not explicitly evaluated δ. We do find, however, that (4.25) describes the results of our numerical simulations very well, if we choose a large value of δ. For a defocusing medium, $G = 2$, we have $\gamma = 0.707$ and choosing $\delta = 500$ gives excellent agreement with numerics, as shown in Fig. 7. In fact the quintic saturation is so strong that the region of subcriticality is narrower than we can detect numerically.

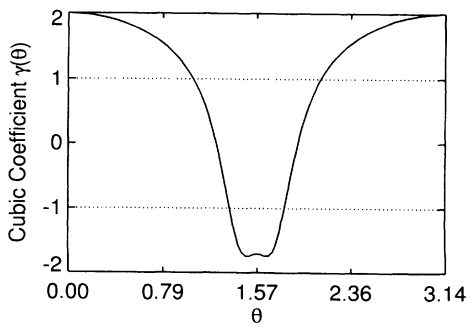

FIG. 6. The cubic coefficient γ as a function of the angle θ between the two modes A_1 and A_2, for a self-defocusing medium with $G = 2$.

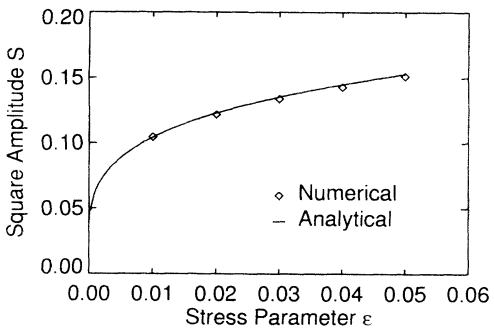

FIG. 7. Square amplitude for a self-defocusing medium ($D < 0$) with $G = 2$. The numerical curve is generated by simulation in two transverse dimensions.

V. NUMERICAL SIMULATIONS

Previous simulations in one transverse dimension [23] verified the correctness of the linear analysis. As we have just demonstrated, however, it is vital to extend the simulations into the second transverse dimension. This was recently done for the case of Gaussian input beams and self-focusing media, and the spontaneous appearance of seemingly stable hexagonal patterns in the high-intensity center of the beams was confirmed [24].

We have undertaken much more extensive and definitive simulations employing periodic boundary conditions to simulate plane-wave excitation. For self-focusing media, the results confirm that hexagons are preferred, and persist some way below the linear instability threshold, much as in the previously discussed systems. For self-defocusing media, no previous simulations in two transverse dimension have been published, so the emergence of square patterns (which are rather stable) is unexpected.

The numerical method used in these computations was a modified beam propagation algorithm, typically on a $64 \times 64 \times 20$ computational grid with a $128 \times 128 \times 40$ grid used as a check. The operator was split into diffraction and plane-wave propagation. The diffraction propagation was performed spectrally using the fast Fourier transform to convert from spatial to spectral coordinates. The remaining operator was integrated so as to enforce the conservation law (2.3) numerically. Figure 8 shows the characteristics of the system. Along those characteristics, only the phases of the corresponding fields change. Integrating for that phase change yields

$$F_j^{n+1} = F_{j-1}^n \exp\left(iD \int |F|^2 + G|B|^2 \right)$$
$$\approx F_{j-1}^n \exp(iD|F_{j-1}^n|^2 dz) \exp\left(iDG(|B_{j-1}^n|^2 + 4|B_j^n|^2 + |B_{j+1}^n|^2)dz/6\right), \tag{5.1}$$
$$B_j^{n+1} = B_{j+1}^n \exp\left(iD \int G|F|^2 + |B|^2 \right)$$
$$\approx B_{j+1}^n \exp(iD|B_{j+1}^n|^2 dz) \exp\left(iDG(|F_{j-1}^n|^2 + 4|F_j^n|^2 + |F_{j+1}^n|^2)dz/6\right), \tag{5.2}$$

where the integrals are along the characteristics for F and B, respectively. The phase is accurate to third order, and the amplitude is exact. The overall accuracy of the scheme is second order due to the splitting error, but enforcing the conservation law (2.3) leads to excellent results even with coarse sampling [37].

In all simulations we initially fill the medium with the homogeneous plane-wave solution (2.4), and apply input plane waves with low-level random noise across the transverse plane. We maintain this noise for several transit times otherwise it would propagate out of the slab in just one transit and the instability would develop very slowly. We run the simulation long enough for a pattern to emerge (typically 40 transits) and saturate (about 150 transits), although it may not always become stationary (in time). We then explore parameter space by varying D and restarting the computation, using the final state of the previous simulation as an initial condition.

The results of our simulations are summarized in Fig. 9 in the (D, G) plane, together with curves of minimum threshold in each quadrant. As expected we observe hexagons for $DG > 0$ and squares for $DG < 0$. These patterns were all obtained at 10% above threshold with $|G|$=2. Note that in the third quadrant the hexagonal pattern is inverted, a honeycomb structure rather than the bright spots as in the first (physical) quadrant.

For self-focusing media the hexagons persist below the linear stability threshold, as indicated in Fig. 3. Indeed for both $G = 1$ and $G = 2$ they finally lose stability to the plane-wave solution (2.4) at $\approx 15\%$ below threshold, which can be attributed to the large quadratic interaction coefficient σ. One intriguing feature we have observed in this case is that there is a Hopf bifurcation, on the otherwise stable hexagon branch, close to the linear instability

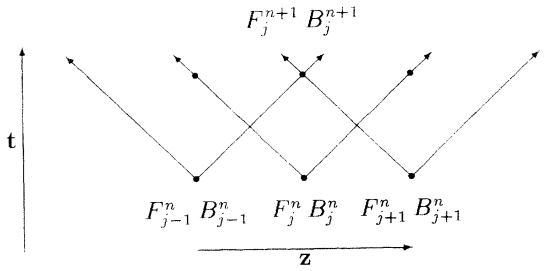

FIG. 8. Characteristics for the counterpropagating system. The index j represents the z position on the mesh while the index n represents the t position on the mesh.

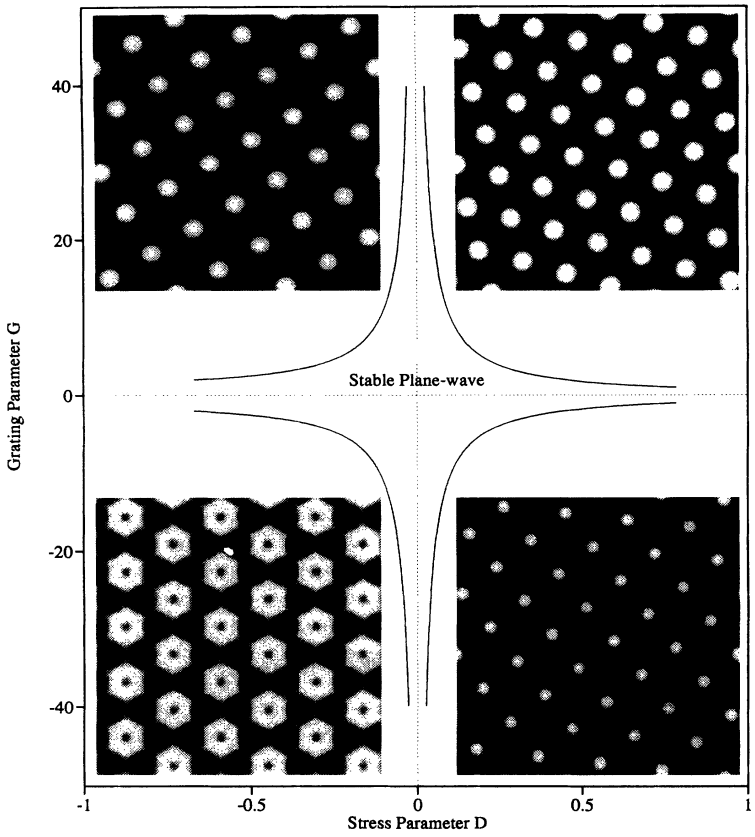

FIG. 9. Typical patterns generated by numerical simulation. The solid lines represent the neutral curves in the (D, G) plane. Each pattern represents the amplitude of the forward field F as it exits the Kerr slab. Gray scale, from white (high intensity) to black (low intensity), is used. These patterns were each generated for $|G| = 2$ at 10% above the linear instability threshold.

threshold. This bifurcation leads to a dynamic exchange of energy between two types of hexagons. The first has a wavelength corresponding to k=k_c while the other corresponds to k=$\sqrt{3}k_c$. In fact the hexagon at k=$\sqrt{3}k_c$ is driven by the hexagon at k=k_c through the interaction of the modes A_1 and A_2 which results in a wave number $\mathbf{k} = \mathbf{k}_1 + \mathbf{k}_2$, $|\mathbf{k}| = \sqrt{3}k_c$. The numerical results show that the new amplitude is not slaved to the amplitude of the fundamental hexagon but in deriving the amplitude equation (4.5) this slaving assumption is implicit since we take as our linear solution only modes with wave number k_c. If we include modes with wave number $|\mathbf{k}| = \sqrt{3}k_c$ as part of our linear solution and write down phenomenological amplitude equations for their interaction with modes at $|\mathbf{k}| = k_c$, then the resulting dynamical system displays a Hopf bifurcation, as shown in Fig. 10. The reason for allowing modes with $k \neq k_c$ to become "active" is simple. The intertwining curves in Fig. 2 demonstrate that many wave numbers are only weakly damped with respect to the growth of modes at $k = k_c$. A resonant interaction, such as $\mathbf{k}_1 + \mathbf{k}_2$, allows this weak damping to be overcome, hence the Hopf bifurcation.

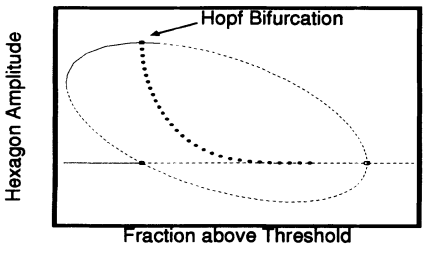

FIG. 10. Evidence of a Hopf bifurcation for a self-focusing medium ($D > 0$), where the underlying pattern is hexagonal. The solid dots represent the minimum of the resulting periodic solution.

For self-defocusing media all our simulations resulted in the observation of very stable square patterns. Actually we use the term "square" rather loosely since our discrete grid is not capable of discerning a square from a nearly-square rhombus. As mentioned earlier the squares saturate strongly at quintic order, but the reason for this is unclear at present.

VI. CONCLUSION

In summary, counterpropagation in a slab of nonlinear material, which is at the heart of many lasers and nonlinear optical systems, presents a very rich and challenging problem in the elucidation, interpretation, and simulation of spatial patterns.

Analytical results conform to related systems in certain respects, but the nonlinear behavior, as yet not fully explored, already displays interesting and unusual features. The hexagon-square dichotomy is one such feature; another is the presence of the Hopf bifurcation, on what would normally be a stable region of the hexagon branch. Many other features remain to be studied, not least the nonlinear behavior for vector fields in cases where the polarization instability discussed above is close enough

to the amplitude instability threshold to require a vector field treatment. Matching simulations to experiments will involve still more complications, such as finite time response and finite beam width.

On the simulation side, though smooth constant input beams have been shown to develop spatial or spatiotemporal structures through interaction with Kerr media, computer simulation is stretched when three, or even four, independent variables must be tracked over substantial ranges of these variables. To help both experimentalists and simulators, there is a need for effective analytic techniques to deal with finite, and even narrow, optical beams — small aspect-ratio systems, as they would be termed in fluids.

Some comments as to optimum conditions for observation of these phenomena are appropriate. This is particularly so for the predicted square patterns, since the hexagonal strucures already have some experimental support in atomic vapor experiments [16]. Vapors are not likely to show squares, however, because atomic diffusion is likely to wash out the grating term which is essential for square formation in the present model.

Semiconductors are worth considering, because they show very large negative Kerr coefficients [39]. Again there is a problem in that carrier diffusion will normally annul the grating, but an interesting way around the problem exists if quantum-well material is used. In such materials the photoexcited electrons and holes are confined within wells much narrower than the optical wavelength, and so if the wells are such that the confinement is in the direction of optical propagation (which is the normal configuration), then the grating factor should be close to its maximum value. Transverse diffusion may be quite large in these materials, but this should not have a significantly deleterious effect on pattern formation, at least in broad beams.

Many of the phenomena discussed have close similarities with fluid patterns, particularly hexagons and their defects. Optics does, however, offer some advantages over fluids. That optics has a speed advantage is self-evident: optical systems are often very fast, even embarassingly so for the purposes of observation. That fact is not particularly relevant to pattern formation, however. Perhaps the most important advantage of optics over fluids is that most nonlinear optical systems have, at least in principle, a quantum description, and there is a possibility of addressing the interface between classical and quantum patterns. For example, it has recently been pointed out [5,38], that there is a Heisenberg-type uncertainty principle between the near- and far-field patterns. This ultimately arises from the optical phase, which is a classical remnant of a quantum variable.

One other potential advantage of optics over fluids is that it may be possible to form very small-scale patterns. This would be of interest if the objective is to apply the pattern-forming properties to information storage or processing [40]. How, then, do the patterns described above scale? The transverse scale is determined by the thickness of the slab, so that small-scale patterns could be achieved by using very thin slabs. Of course this also requires an increase in intensity to maintain the nonlinear phase shift. Interestingly, these two scalings combine in such a way that the *power* to generate a pattern with a given number of spots (pixels) is independent of the scale of the pattern (and is determined just by n_2 and the wavelength). Since the time scales will also go down with the length scales, there is some possibility of using pulsed excitation to achieve pattern formation, e.g., in semiconductors, if continuous wave excitation is too weak or causes thermal problems. Ultimately, it may be necessary to go beyond the paraxial limit on which our model is based, but there is no reason to doubt that wavelength scale pattern formation may be possible.

ACKNOWLEDGMENTS

We wish to thank the Arizona Center for Mathematical Sciences (ACMS) for support. ACMS is sponsored by AFOSR Contract No. FQ8671-9000589 (AFOSR-90-0021) with the University Research Initiative Program at the University of Arizona. This research was also supported by SERC under Grants No. GR/F 49811, No. GR/F 75087, No. GR/G 12665, and No. GR/G 15031, and under a Twinning Programme of the European Communities. Financial support from NATO is also gratefully acknowledged. We also thank E. M. Wright, A. C. Newell, G. Luther, and G. McDonald for interesting and fruitful discussions.

APPENDIX A: MODEL EQUATIONS

For analytical convenience we tranform (2.7) into (2.9) through the change of basis (2.8). The matrix J which premultiplies $\partial_t \mathbf{U}$ is given by

$$J = \begin{bmatrix} 0 & I \\ I & 0 \end{bmatrix}, \quad I = \begin{bmatrix} 1 & 0 \\ 0 & 1 \end{bmatrix}. \tag{A1}$$

The linear operator $\mathcal{L}$ is defined by

$$\mathcal{L} = \partial_z - M, \quad M = \begin{bmatrix} M_1 & 0 \\ 0 & M_2 \end{bmatrix}, \tag{A2}$$

where the components of M are

$$M_1 = \begin{bmatrix} 0 & -\beta\nabla^2 \\ \beta\nabla^2 - 2D(G-1) & 0 \end{bmatrix}, \quad M_2 = \begin{bmatrix} 0 & -\beta\nabla^2 \\ \beta\nabla^2 + 2D(G+1) & 0 \end{bmatrix}. \tag{A3}$$

The quadratic nonlinear terms in (2.7) transform to give

$$\mathcal{N}_1(\mathbf{U}|\mathbf{U}) = \frac{1}{2}\begin{bmatrix} (G-1)U_1U_4 - (1+G)U_2U_3 \\ (1-G)U_2U_4 + (3-G)U_1U_3 \\ (G-1)U_1U_2 - (G+1)U_3U_4 \\ ((3-G)U_1U_1 + (1+G)U_2U_2 + 3(1+G)U_3U_3 + (1+G)U_4U_4)/2 \end{bmatrix}, \tag{A4}$$

while the cubic nonlinear terms become

$$\mathcal{N}_2(\mathbf{U}|\mathbf{U}|\mathbf{U}) = \frac{1}{16}\begin{bmatrix} -(U_1U_1 + U_2U_2 + U_3U_3 + 3U_4U_4)U_2 - 2U_1U_3U_4 \\ (U_1U_1 + U_2U_2 + U_4U_4 + 3U_3U_3)U_1 + 2U_2U_3U_4 \\ -(U_1U_1 + U_3U_3 + U_4U_4 + 3U_2U_2)U_4 - 2U_1U_2U_3 \\ (U_2U_2 + U_3U_3 + U_4U_4 + 3U_1U_1)U_3 + 2U_1U_2U_4 \end{bmatrix}$$
$$+\frac{G}{16}\begin{bmatrix} -(U_1U_1 + U_2U_2 + U_3U_3 - U_4U_4)U_2 + 2U_1U_3U_4 \\ (U_1U_1 + U_2U_2 + U_4U_4 - U_3U_3)U_1 - 2U_2U_3U_4 \\ -(U_1U_1 + U_3U_3 + U_4U_4 - U_2U_2)U_4 + 2U_1U_2U_3 \\ (U_2U_2 + U_3U_3 + U_4U_4 - U_1U_1)U_3 - 2U_1U_2U_4 \end{bmatrix}.$$

APPENDIX B: LINEAR ANALYSIS

The transformation to the new basis, detailed in Appendix A, allows us to explicitly construct the solutions of (3.4). For the M_j defined in (3.4) we need to calculate $\exp(M_j z)$. The off-diagonal nature of M_j means that

$$M_j^2 = -\psi_j^2 I. \tag{B1}$$

To make use of this we write $\exp(M_j z)$ in the form

$$\exp(M_j z) = \left(I - \frac{\psi_j^2 z^2}{2!} + \frac{\psi_j^4 z^4}{4!} - \cdots\right) + \frac{M_j}{\psi_j}\left(\psi_j z - \frac{\psi_j^3 z^3}{3!} + \cdots\right), \tag{B2}$$

which allows us to write

$$\exp(M_j z) = \cos(\psi_j z) + \frac{M_j}{\psi_j}\sin(\psi_j z). \tag{B3}$$

The final result is

$$\exp(M_j z) = \begin{bmatrix} \cos(\psi_j z) & \dfrac{\beta k^2}{\psi_j}\sin(\psi_j z) \\ -\dfrac{\psi_j}{\beta k^2}\sin(\psi_j z) & \cos(\psi_j z) \end{bmatrix}. \tag{B4}$$

Now we prove the result that one group of neutral stability curves ($H_1 = 0$) has solutions which have odd symmetry in z ($\rho = -1$) while the other group ($H_2 = 0$) has solutions with even symmetry in z ($\rho = +1$). First we will prove that if $H_1 = 0$ and $H_2 \neq 0$ then $\rho = -1$. To do so we evaluate (3.5) at $z = 1/2$,

$$\mathbf{u}(1/2) = \begin{bmatrix} \exp(M_1) & 0 \\ 0 & \exp(M_2) \end{bmatrix}\mathbf{u}(-1/2). \tag{B5}$$

Using the symmetry in (3.16) we find that

$$\begin{bmatrix} \exp(M_1) & 0 \\ 0 & \exp(M_2) \end{bmatrix}\mathbf{u}(-1/2) = \rho P\mathbf{u}(-1/2), \tag{B6}$$

and on applying the boundary conditions (3.3) we obtain

$$\tfrac{1}{2}Q(\exp(M_1) - \exp(M_2))\mathbf{v}(-1/2). = \rho\mathbf{v}(-1/2). \tag{B7}$$

This is an eigenvalue problem in ρ and we already know that $\rho = \pm 1$. The corresponding eigenvectors are given in (3.14). Substituting these into (B7) results in

$$\left(\frac{\sin(\psi_1)}{\psi_1} + \frac{\sin(\psi_2)}{\psi_2}\right)\rho = \cos(\psi_2)\frac{\sin(\psi_1)}{\psi_1} - \cos(\psi_1)\frac{\sin(\psi_2)}{\psi_2}. \tag{B8}$$

Now we assume that we are on a neutral curve defined by $H_1 = 0$, which implies that

$$\cos(\psi_1/2)\cos(\psi_2/2) = -\frac{\psi_1}{\psi_2}\sin(\psi_1/2)\sin(\psi_2/2). \tag{B9}$$

Replacing (B9) into (B8) leads, after some algebra, to the result that $\rho = -1$. Note that to use the eigenvectors in (3.14) we had to assume that $H_2 \neq 0$, i.e., we are not at a crossing point. The corresponding proof that $H_2 = 0$ implies $\rho = +1$ is very simple. If we make the transformation $\psi_1 \to \psi_2$ in (B8) then $\rho \to -\rho$. Since $H_1 = 0 \Rightarrow \rho = -1$ then $H_2 = 0 \Rightarrow \rho = +1$ because $\psi_1 \to \psi_2 \Rightarrow H_1 \to H_2$.

Finally in this Appendix, we would like to prove the result that on increasing $|D|$ we first cross a neutral curve defined by $H_2 = 0$ if $DG > 0$ and $H_1 = 0$ if $DG < 0$, for positions sufficiently close to the optical axis (k=0). The proof is outlined below.

If $D = 0$ then $\psi_1 = \psi_2 = \beta k^2$ and $H_1 = H_2 = 1$. Choose k^2 such that $\beta k^2 < \pi$. Expand the terms in (3.10) for small D and it becomes clear that

$$H_1 \simeq 1 + \frac{2DG}{\beta k^2}\sin^2(\beta k^2/2),$$
$$H_2 \simeq 1 - \frac{2DG}{\beta k^2}\sin^2(\beta k^2/2). \tag{B10}$$

If $DG > 0$ then H_1 increases while H_2 decreases. If $DG < 0$ then H_1 decreases while H_2 increases. To prove that the function that is initially decreasing actually passes through zero first we will show that the functions next meet when they are both negative. From (3.11) we see that for $H_1 = H_2$ we require that $\psi_i = 2m\pi$, $m = 1, 2, \ldots$. Assuming $G \notin [-1, 1]$ then increasing $|DG|$ (holding G fixed) increases either ψ_1^2 or ψ_2^2 while the other decreases. When the increasing one passes through 2π then $H_1 = H_2$. Say $\psi_i = 2\pi$. At this point we have from (3.11)

$$H_1 = H_2 = \cos(\psi_i/2)\cos(\psi_j/2) = -\cos(\psi_j/2) < 0,$$

since ψ_j started out less than π and continued to decrease. Thus both H_1 and H_2 passed through zero and the one that started off decreasing must have passed through zero first. Hence if $DG > 0$ we have $H_2 \to 0$ first while if $DG < 0$ we have $H_1 \to 0$ first.

We have shown which curve we cross for small k, but it could happen that the curves cross themselves before reaching a minimum. It turns out, however, that a line from the origin to the first crossing point is tangential, at the point where the curves cross, to the first curve crossed for small k and hence that curve must also be the minimum. As mentioned in the text, in most cases this is also the curve with the lowest threshold $|D|$ and thus defines the critical point.

APPENDIX C: NONLINEAR ANALYSIS

In order to calculate the amplitude equations for the counterpropagating system we need to expand the governing equations (2.9) in terms of the stress parameter ϵ. Given the scalings shown in (4.1), (4.2), and (4.4) we obtain

$$J\partial_t \mathbf{U} = J(\epsilon\partial_{T_1} + \epsilon^2\partial_{T_2} + \cdots)(\epsilon^{1/2}\mathbf{U}^{(0)} + \epsilon\mathbf{U}^{(1)} + \cdots) = \epsilon^{3/2}J\partial_{T_1}\mathbf{U}^{(0)} + \cdots , \tag{C1}$$

$$\begin{aligned}\mathcal{L}\mathbf{U} &= (\mathcal{L}^{(0)} - \epsilon\mathcal{L}^{(1)} + \cdots)(\epsilon^{1/2}\mathbf{U}^{(0)} + \epsilon\mathbf{U}^{(1)} + \epsilon^{3/2}\mathbf{U}^{(2)} + \cdots) \\ &= \epsilon^{1/2}\mathcal{L}^{(0)}\mathbf{U}^{(0)} + \epsilon\mathcal{L}^{(0)}\mathbf{U}^{(1)} + \epsilon^{3/2}(\mathcal{L}^{(0)}\mathbf{U}^{(2)} - \mathcal{L}^{(1)}\mathbf{U}^{(0)}) + \cdots ,\end{aligned} \tag{C2}$$

$$\begin{aligned}D\mathcal{N}_1(\mathbf{U}|\mathbf{U}) &= D_c(1+\epsilon)\,\mathcal{N}_1\big((\epsilon^{1/2}\mathbf{U}^{(0)} + \epsilon\mathbf{U}^{(1)} + \cdots)|(\epsilon^{1/2}\mathbf{U}^{(0)} + \epsilon\mathbf{U}^{(1)} + \cdots)\big) \\ &= \epsilon D_c\mathcal{N}_1(\mathbf{U}^{(0)}|\mathbf{U}^{(0)}) + \epsilon^{3/2}D_c(\mathcal{N}_1(\mathbf{U}^{(0)}|\mathbf{U}^{(1)}) + \mathcal{N}_1(\mathbf{U}^{(1)}|\mathbf{U}^{(0)})) + \cdots ,\end{aligned} \tag{C3}$$

$$\begin{aligned}D\mathcal{N}_2(\mathbf{U}|\mathbf{U}|\mathbf{U}) &= D_c(1+\epsilon)\,\mathcal{N}_2\big((\epsilon^{1/2}\mathbf{U}^{(0)} + \cdots)|(\epsilon^{1/2}\mathbf{U}^{(0)} + \cdots)|(\epsilon^{1/2}\mathbf{U}^{(0)} + \cdots)\big) \\ &= \epsilon^{3/2}D_c\mathcal{N}_2(\mathbf{U}^{(0)}|\mathbf{U}^{(0)}|\mathbf{U}^{(0)}) + \cdots ,\end{aligned} \tag{C4}$$

where the important linear term $\mathcal{L}^{(1)}$ is given by

$$\mathcal{L}^{(1)} = -\left.\frac{\partial\mathcal{L}}{\partial\epsilon}\right|_{\epsilon=0} = \left.\frac{\partial M}{\partial\epsilon}\right|_{\epsilon=0} = \left.\begin{bmatrix} \partial M_1/\partial\epsilon & 0 \\ 0 & \partial M_2/\partial\epsilon \end{bmatrix}\right|_{\epsilon=0}. \tag{C5}$$

The matrix M was given in Appendix A and a simple calculation reveals that

$$\left.\frac{\partial M_1}{\partial\epsilon}\right|_{\epsilon=0} = \begin{bmatrix} 0 & 0 \\ 2D_c(1-G) & 0 \end{bmatrix}, \quad \left.\frac{\partial M_2}{\partial\epsilon}\right|_{\epsilon=0} = \begin{bmatrix} 0 & 0 \\ 2D_c(G+1) & 0 \end{bmatrix}. \tag{C6}$$

[1] M. C. Cross and P. C. Hohenberg, Rev. Mod. Phys. **65**, 851 (1993).
[2] A. C. Newell, T. Passot, and J. Lega, Annu. Rev. Fluid Mech. **25**, 399 (1993).
[3] L. A. Lugiato, Phys. Rep. **219**, 293 (1992).
[4] C. O. Weiss, Phys. Rep. **219**, 311 (1992).
[5] L. A. Lugiato and F. Castelli, Phys. Rev. Lett. **68**, 3284 (1992).
[6] S. Maneuf, R. Desailly, and C. Froehly, Opt. Commun. **65**, 193 (1988).
[7] S. Maneuf and F. Renaud, Opt. Commun. **66**, 325 (1988).
[8] J. S. Aitchison, A. M. Weiner, Y. Silverberg, M. K. Oliver, J. L. Jackel, D. E. Leaird, E. M. Vogel, and P. W. Smith, Opt. Lett. **15**, 471 (1990).
[9] G. A. Schwartzlander, Jr., D. R. Anderson, J. J. Regan, H. Yin, and A. E. Kaplan, Phys. Rev. Lett. **66**, 1583 (1991).
[10] P. Coullet, L. Gil, and F. Rocca, Opt. Commun. **73**, 403 (1989).
[11] L. Gil, K. Emilsson, and G.-L. Oppo, Phys. Rev. A **45**, 567 (1992).
[12] G. D'Alessandro and W. J. Firth, Phys. Rev. Lett. **66**, 2597 (1991).
[13] G. D'Alessandro and W. J. Firth, Phys. Rev. A **46**, 537 (1992).
[14] R. Macdonald and H. J. Eichler, Opt. Commun. **89** 289 (1992).
[15] M. Tamburrini, M. Bonavita, S. Wabnitz, and E. San-

tamato, Opt. Lett. **18**, 855 (1993).
[16] G. Grynberg , E. Le Bihan, P. Verkerk, P. Simoneau, J. R. R. Leite, D. Bloch, S. Le Boiteux, and M. Ducloy, Opt. Commun. **67**, 363 (1988).
[17] A. Petrossian, M. Pinard, A. Maître, J. Y. Courtois, and G. Grynberg, Europhys. Lett. **18**, 690 (1992).
[18] G. Grynberg, Opt. Commun. **66**, 321 (1988).
[19] J. Y. Courtois and G. Grynberg, Opt. Commun. **97**, 186 (1992).
[20] B. Thuering, R. Neubecker, and T. Tschudi, Opt. Commun. **102**, 111 (1993).
[21] E. Pampaloni, S. Residori, and F. T. Arecchi, Europhys. Lett. **24**, 647 (1993).
[22] W. J. Firth and C. Paré, Opt. Lett. **13**, 1096 (1988).
[23] W. J. Firth, A. Fitzgerald, and C. Paré, J. Opt. Soc. Am. B **7**, 1087 (1990).
[24] R. Chang, W. J. Firth, R. Indik, J. V. Moloney, and E. M. Wright, Opt. Commun. **88**, 167 (1992).
[25] W. J. Firth and C. Penman, Opt. Commun. **94**, 183 (1992).
[26] A. L. Gaeta, R. W. Boyd, J. R. Ackerhalt, and P. W. Milonni, Phys. Rev. Lett. **58**, 2432 (1987).
[27] D. J. Gauthier, M. S. Malcuit, and R. W. Boyd, Phys. Rev. Lett. **61**, 1827 (1988).
[28] W. J. Firth, Opt. Commun. **39**, 343 (1981).
[29] G. P. Agrawal, Phys. Rev. Lett. **59**, 880 (1987).
[30] A. C. Newell, *Solitons in Mathematics and Physics* (SIAM, Philadelphia, 1987).
[31] S. N. Vlasov and V. I. Talanov, *Optical Phase Conjugation in Nonlinear Media*, edited by V. I. Bespalov (Institute of Applied Physics, USSR Academy of Sciences, Gorki, 1979).
[32] G. G. Luther, Ph.D. thesis, University of Rochester, 1991.
[33] G. G. Luther and C. J. McKinstrie, J. Opt. Soc. Am. B **7**, 1125 (1990).
[34] I. Stakgold, *Greens Functions and Boundary Value Problems* (Wiley-Interscience, New York, 1979).
[35] S. Ciliberto, P. Coullet, J. Lega, E. Pampaloni, and C. Perez-Garcia, Phys. Rev. Lett. **65**, 2370 (1990).
[36] P. Coullet, L. Gil, and D. Repaux, Phys. Rev. Lett. **62**, 2957 (1989).
[37] C. W. Gear, Physica D **60**, 303 (1992).
[38] G. Grynberg and L. A. Lugiato, Opt. Commun. **101**, 69 (1993).
[39] D. Weaire, B. S. Wherret, D. A. B. Miller, and S. D. Smith, Opt. Lett. **4**, 331 (1979).
[40] G. S. Mcdonald and W. J. Firth, J. Opt. Soc. Am. B **10**, 1081 (1993).

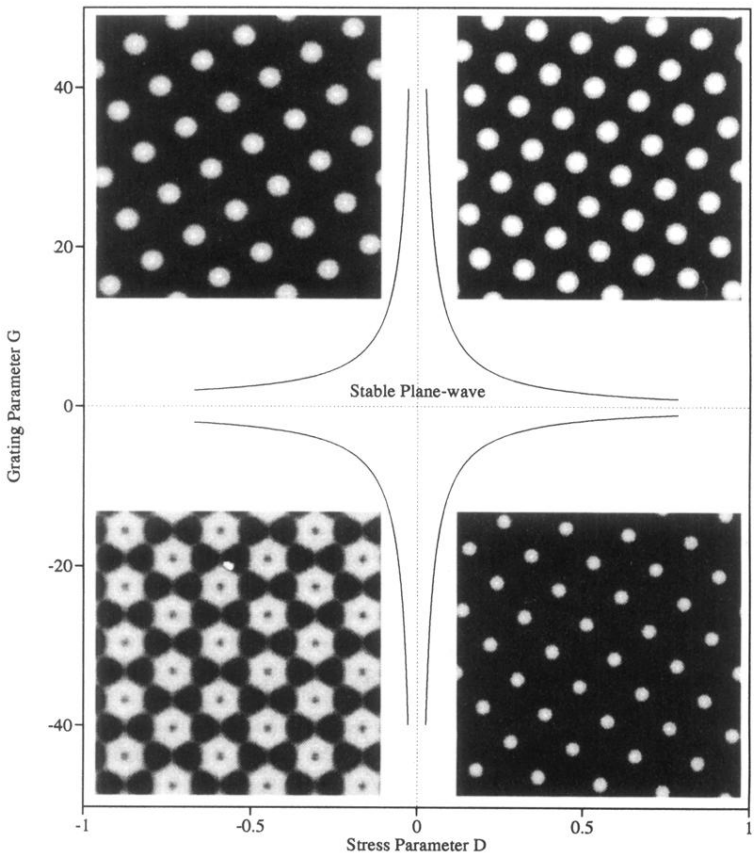

FIG. 9. Typical patterns generated by numerical simulation. The solid lines represent the neutral curves in the (D, G) plane. Each pattern represents the amplitude of the forward field F as it exits the Kerr slab. Gray scale, from white (high intensity) to black (low intensity), is used. These patterns were each generated for $|G| = 2$ at 10% above the linear instability threshold.